# LANGMUIR

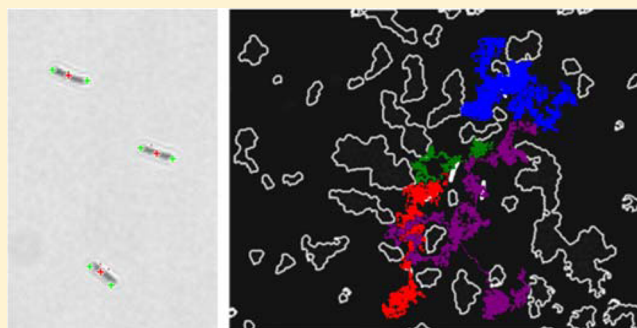# Interfacial and Confined Colloidal Rod Diffusion

Julie L. Bitter,[†] Yuguang Yang,[‡] Gregg Duncan,[‡] Howard Fairbrother,[†] and Michael A. Bevan*[,‡]

[†]Chemistry and [‡]Chemical & Biomolecular Engineering, Johns Hopkins University, Baltimore, Maryland 21218, United States

**ABSTRACT:** Optical microscopy is used to measure translational and rotational diffusion of colloidal rods near a single wall, confined between parallel walls, and within quasi-2D porous media as a function of rod aspect ratio and aqueous solution ionic strength. Translational and rotational diffusivities are obtained as rod particles experience positions closer to boundaries and for larger aspect ratios. Models based on position dependent hydrodynamic interactions quantitatively capture diffusivities in all geometries and indicate particle–wall separations in agreement with independent estimates based on electrostatic interactions. Short-time translational diffusion in quasi-2D porous media is insensitive to porous media area fraction, which appears to arise from a balance of hydrodynamic hindrance and enhanced translation due to parallel alignment along surfaces. Findings in this work provide a basis to interpret and predict interfacial and confined colloidal rod transport relevant to biological, environmental, and synthetic material systems.

## INTRODUCTION

Anisotropic colloidal particles are present in biological, medical, environmental, and synthetic material systems. Transport of anisotropic particles in interfacial and confined geometries is important to problems involving, for example, biological[1−4] and drug[5,6] particle transport within tissues, nanoparticle fate within environmental porous media,[7−12] and deposition and assembly on substrates of particle-based surface coatings.[13−15] Colloidal particle transport near surfaces in general depends on conservative colloidal forces (e.g., electrostatic, van der Waals, gravity) and nonconservative hydrodynamic forces (e.g., Stokes drag, lubrication). Conservative colloidal forces determine how close particles get to surfaces, which determines position dependent hydrodynamic forces that govern how much a particle's motion is impeded by fluid friction. For anisotropic particles, and rod shaped particles, the situation becomes more complex; conservative forces determine both position and orientation, which controls net hydrodynamic interactions as well as coupling between translational and rotational motion.[16]

Colloidal rod diffusion in bulk systems is reasonably well understood based on close correspondence between models[17−20] and measurements.[21−24] Likewise, position dependent diffusion of spherical colloids adjacent to surfaces has also been shown in high resolution measurements[25−29] to agree with models that self-consistently consider conservative and nonconservative colloidal forces.[30,31] However, analysis of measured colloidal rod diffusion near boundaries[3,32−35] has been restricted based on the limitations of available models. For example, many studies have used numerical results for bulk rod diffusion[17−20] modified by approximate lubrication corrections for cylinders adjacent to single planar wall surfaces.[36] Models of colloidal rods as "chains-of-spheres" more accurately consider position and orientation dependent hydrodynamic interactions,

but the results are limited to a single aspect ratio and a single wall surface.[37] In short, easy-to-use, parametric, experimentally validated models are not currently available to interpret and predict boundary effects on colloidal rod diffusion.

In this work, we use optical microscopy to measure translational and rotational diffusion of colloidal rods versus aspect ratio, solution ionic strength, and geometries (Figure 1). We investigate gold (Au) rods with cross-sectional diameters of $d = 2a = 300$ nm and lengths of $L \approx 2−6$ $\mu$m to probe aspect ratios of $p = L/d \approx 7−20$. Rod-wall geometries studies include (1) particles levitated above single planar wall surfaces via a balance of gravity and electrostatic repulsion, (2) particles confined in a quasi-two-dimensional gap between two nominally parallel walls in a slit pore geometry, and (3) particles confined within a quasi-two-dimensional porous media that is formed by 2 $\mu$m spherical silica colloid spacers in random amorphous configurations at different area fractions. The solution ionic strength is varied from the minute ionic strength of deionized water (0.03 mM) up to 5 mM NaCl, to mediate electrostatic repulsion and the average rod–wall separation distance (without causing deposition or contact). Measured diffusivities are compared to a recent model developed by us[38] using a Stokesian dynamic method of computing diffusion tensors for rigid chains-of-spheres near surfaces. In particular, closed-form expressions fit to computational simulations for translational and rotational diffusivities are compared to experimental measurements as a function of rod–wall separation and rod aspect ratio.
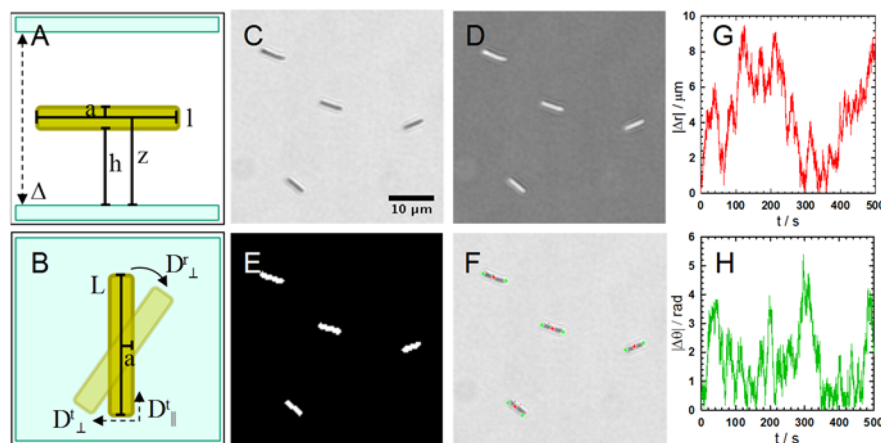
**Figure 1.** Rod-wall schematics, image analysis, and raw trajectories. Schematics of colloidal rod particle adjacent to planar surface with defined variables from (A) side and (B) top views. Representative images of Au colloidal rods and depiction of key image analysis steps showing (C) raw transmitted light image, (D) inversion, (E) binary thresholding, and (F) center and end point labeling. Plots of magnitude of displacement of center of mass position (G) and angular orientation (H) with respect to origin in laboratory coordinates for a single rod particle, corresponding to labels from (F).

## ■ THEORY

**Bulk Translational and Rotational Diffusion.** The translational diffusivity of an isolated rod particle far from any boundaries with long axis, $L$, and diameter, $d = 2a$, can be expressed in terms of its aspect ratio, $p = L/d$ (Figure 1). Expressions reported here, for the bulk diffusion of chains-of-spheres,[38] agree with established models of Tirado and co-workers for cylindrical particles.[19,39,40] The diffusion coefficient for translational diffusion parallel to the long axis is given by[38]

$$D_\parallel^{t,b}(p) = (kT/2\pi\eta L)f_\parallel^{t,b}(p) \tag{1}$$

where

$$f_\parallel^{t,b}(p) = \ln(p) + \frac{-0.4536p^2 - 1.772p + 41.5}{p^2 + 34.38p + 18.96} \tag{2}$$

and the coefficient for translational diffusion perpendicular to the long axis is given by

$$D_\perp^{t,b}(p) = (kT/2\pi\eta L)f_\perp^{t,b}(p) \tag{3}$$

where

$$f_\perp^{t,b}(p) = \ln(p) + \frac{-0.3604p^2 + 28.36p + 72.63}{p^2 + 36.29p + 34.9} \tag{4}$$

and $\eta$ is the fluid medium viscosity, $k$ is Boltzmann's constant, and $T$ is absolute temperature. The three-dimensional center of mass translational diffusion coefficient is given by

$$D^{t,b}(p) = (1/3)D_\parallel^{t,b}(p) + (2/3)D_\perp^{t,b}(p) \tag{5}$$

The rotational diffusivity of an isolated rod particle perpendicular its long axis is given by

$$D_\perp^{r,b}(p) = (3kT/\pi\eta L^3)f_\perp^{r,b}(p) \tag{6}$$

$$f_\perp^{r,b}(p) = \ln(p) + \frac{-1.373p^3 - 19.39p^2 - 148.1p + 265.2}{p^3 + 56.43p^2 + 54.35p - 268.4} \tag{7}$$

**Interfacial Translational and Rotational Diffusion.** Here we summarize expressions for diffusion of chains of spheres as a function of distance relative to a planar interface when the chain's long axis is oriented parallel to the interface.[38] The results converge to the bulk diffusivities in eqs 1−7 for large separations, and to asymptotic results for infinitely long cylinders near a wall[36] at vanishing separations. The

translational diffusivity of a rod particle parallel to its long axis and parallel to a no-slip planar interface, for $h < a$ and $6 < p < 16$, is given by

$$D_\parallel^{t,i}(p, h) = D_\parallel^{t,b}(p)g_\parallel^{t,i}(h) \tag{8}$$

where using the definition for $z = h + a$ (see Figure 1), the function $g(h)$ is given as

$$g_\parallel^{t,i}(h) = \frac{0.9909(z/a)^3 + 0.3907(z/a)^2 - 0.1832(z/a) - 0.001815}{(z/a)^3 + 2.03(z/a)^2 - 0.3874(z/a) - 0.07533} \tag{9}$$

and the coefficient for translational diffusion perpendicular to the long axis, again for $h < a$ and $6 < p < 16$, is given by

$$D_\perp^{t,i}(p, h) = D_\perp^{t,b}(p)g_\perp^{t,i}(h) \tag{10}$$

where

$$g_\perp^{t,i}(h) = \frac{0.9888(z/a)^3 + 0.788(z/a)^2 - 0.207(z/a) - 0.004766}{(z/a)^3 + 3.195(z/a)^2 - 0.09612(z/a) - 0.1523} \tag{11}$$

and the two-dimensional center of mass translation diffusion coefficient at a given surface to surface separation is given by

$$D^{t,i}(p, h) = (1/2)D_\parallel^{t,i}(p, h) + (1/2)D_\perp^{t,i}(p, h) \tag{12}$$

The rotational diffusivity of a rod shaped particle perpendicular its long axis as a function of its aspect ratio and height above the planar surface, interface, for $h < a$ and $6 < p < 16$, is given by

$$D_\perp^{r,i}(p, h) = D_\perp^{r}(p)g_\perp^{r,i}(h) \tag{13}$$

where

$$g_\perp^{r,i}(h) = \frac{0.998(z/a)^3 + 131.1(z/a)^2 + 21.25(z/a) + 0.01275}{(z/a)^3 + 128.7(z/a)^2 + 121.1(z/a) + 2.897} \tag{14}$$

**Confined Translational and Rotational Diffusion.** For a single colloid confined between two parallel planar surfaces with separation, $\delta$, the hydrodynamic hindrance to lateral diffusion can be described using

$$D^{2w}(z, a, \delta) = D^b f^{2w}(z, a, \delta) \tag{15}$$

where a number of approximate solutions exist for $f^{2w}(z,a,\delta)$. The simplest of these is the linear superposition approximation (suggested

by Oseen),[41] which includes hydrodynamic hindrance of each wall from the single wall results as given by

$$f^{2w}(z, a, \delta) = [f^{1w}(z, a)^{-1} + f^{1w}(\delta - z, a)^{-1} - 1]^{-1} \quad (16)$$

which can be applied with any of the separation-dependent diffusivities in eqs 1−14.

**Measured Average Diffusion Coefficients.** Measurements of average diffusivities can be obtained via mean squared positional displacements (MSPD), in one-dimension, $\langle x^2 \rangle$ (or $\langle y^2 \rangle$), as

$$\langle x^2 \rangle = \frac{1}{N_p} \sum_{i=1}^{N_p} [x_i(t) - x_i(0)]^2 = 2\langle D^t \rangle t + \Delta^2 \quad (17)$$

or in polar coordinates, $\langle r^2 \rangle$ (where $r^2 = x^2 + y^2$), as

$$\langle r^2 \rangle = \frac{1}{N_p} \sum_{i=1}^{N_p} [r_i(t) - r_i(0)]^2 = 4\langle D^t \rangle t + \Delta^2 \quad (18)$$

and for mean squared angular displacements (MSAD), $\langle \theta^2 \rangle$, as

$$\langle \theta^2 \rangle = \frac{1}{N_p} \sum_{i=1}^{N_p} [\theta_i(t) - \theta_i(0)]^2 = 2\langle D^r \rangle t + \Delta^2 \quad (19)$$

where $N_p$ is the number of particles, and $\Delta^2$ is related to the square of the uncertainty in either the particle center position or long-axis orientation due to limited spatial resolution (i.e., the CCD camera pixel size is approximately equal to $\Delta$).

**Potential Energy Profiles.** The potential energy for an isolated rod particle with $L$ parallel to an underlying planar surface can be calculated by the sum of contributing potentials as

$$U(z) = U_G(z) + U_E(z) \quad (20)$$

where the subscripts refer to the gravitational (G) and electrostatic (E) interactions, $z = h + a$ is the particle center to the wall surface (Figure 1), $h$ is the particle surface to wall surface separation, and $a$ is the rod short-axis radius. van der Waals attraction is expected to be negligible based on our previous studies of Au−silica interactions.[42]

The gravitational potential energy of each rod depends on its buoyant weight, $G$, as the product of particle volume and density mismatch with the medium as given by

$$U_G(z) = Gz = mg(h + a) = \pi a^2 L(\rho_p - \rho_f) g(h + a) \quad (21)$$

where $m$ is buoyant mass, $g$ is acceleration due to gravity, and $\rho_p$ and $\rho_f$ are particle and fluid densities, respectively. For rods where the potential energy associated with elevating one end relative to the other is >5$kT$, the long axis will remain parallel to the underlying wall. For this orientation, the rod−wall electrostatic interaction depends on the nondimensional double layer thickness. In particular, for thin double layers ($\kappa a \gg 1$) and a 1:1 electrolyte, we consider a solution based on the nonlinear Poison−Boltzmann equation to model the electrostatic double layer on flat plates. Used with the Derjaguin approximation for geometry correction, this gives a potential as[43]

$$U_E^{ND}(z) = 64\pi LB(\kappa a/2\pi)^{0.5} \exp[-\kappa z] \quad (22)$$

where

$$B = \varepsilon \left(\frac{kT}{e}\right)^2 \tanh\left(\frac{e\psi_p}{4kT}\right) \tanh\left(\frac{e\psi_w}{4kT}\right) \quad (23)$$

and

$$\kappa = \left[\frac{e^2 N_A}{\varepsilon kT} \sum_i C_i\right]^{1/2} \quad (24)$$

where $\kappa$ is the inverse Debye screening length, $\varepsilon$ is the solvent dielectric constant, $e$ is the elemental charge, $\psi_p$ and $\psi_w$ are the surface potentials of the particle and the wall, respectively, $N_A$ is Avogadro's number, and $C_i$ is electrolyte molarity.

For thick double layers ($\kappa a \approx 1$) and a 1:1 electrolyte, we approximate the interaction by considering a chain of touching spheres, each of radius, $a$, and total number of $L/a$, and use the linear superposition approximation for sphere−plate interactions[44] to give

$$U_E^{LS}(z) = (L/2a)U_{E,PW}^{LS}(h)$$
$$= (L/2a)16\pi aB \exp(-\kappa z)$$
$$= 8\pi LB \exp(-\kappa z) \quad (25)$$

**Average Particle−Wall Separation and Diffusivities.** Colloidal rods experience Brownian motion and sample a range of heights relative to underlying wall surfaces in the presence of the colloidal interactions and gravity given in eqs 20−25. By considering the balance of electrostatic and gravitational interactions, the rod's most probable elevation, $h_m$, can be determined where the gradient of the potential vanishes (i.e., where the sum of the forces is zero). Using the potential in eq 22, the value of $h_m$ is

$$h_m^{ND} = \kappa^{-1}\ln\left[\frac{64(\kappa^3 a/2\pi)^{0.5}B}{a^2(\rho_p - \rho_f)g}\right] \quad (26)$$

whereas using the potential in eq 25 gives the value of $h_m$ as

$$h_m^{LS} = \kappa^{-1}\ln\left[\frac{8\kappa B}{a^2(\rho_p - \rho_f)g}\right] \quad (27)$$

For comparison, it is also possible to compute the average elevation, $\langle h \rangle$, from the particle−wall interactions by considering the Boltzmann weighted integral average as

$$\langle h \rangle = \frac{\int h p(h)\, dh}{\int p(h)\, dh} \quad (28)$$

where $p(h)$ is the probability of rod−wall separations given by a Boltzmann distribution as

$$p(h) = p(h_m)\exp[-(U(h) - U(h_m))/kT] \quad (29)$$

While the position dependent diffusivities in eqs 1−16 can be evaluated at discrete elevations such as $h_m$ or $\langle h \rangle$ in eqs 26−28, the average diffusivity, $\langle D \rangle$, for each diffusion mode is accurately predicted as an average over the equilibrium distribution of heights sampled by confined particles as given by[25,30,42]

$$\langle D \rangle = \frac{\int D(h)\, p(h)\, dh}{\int p(h)\, dh} \quad (30)$$

## ■ MATERIALS AND METHODS

**Colloids and Surfaces.** Hydrochloric acid, potassium hydroxide, sodium chloride, and colloidal SiO$_2$ (2.34 $\mu$m) were used as received without further purification. Au rods were electrochemically grown to prescribed lengths in 300 nm pores of anodic aluminum oxide membranes (that determine the Au rod diameter from SEM[45]). The alumina template was dissolved in base, and rods were freed from a thin film using nitric acid.[45] Rods were dispersed in deionized water. Zeta potential ($\zeta$) was used as an estimation of the surface potential for the Au rods ($\psi_p$), and was measured at four ionic strength conditions using electrophoretic mobility.

For quasi-2D porous media experiments, dilute silica spacer particle dispersions were prepared by adding 0.5 $\mu$L of the stock to 4 mL of DI water, whereas concentrated dispersions for spin coating were prepared by diluting 100 $\mu$L of stock silica in 1 mL of 0.1 mM NaCl. The addition of NaCl aided in adhering the silica particles to the coverslips during spin coating. Au rod dispersions were prepared by diluting 60 $\mu$L of stock into 136 $\mu$L of electrolyte solution and 4 $\mu$L silica particle spacers. For two-wall experiments, this dispersion was used as is to confine the rods, and for one-wall experiments the dispersion was diluted to achieve the desired ionic strength. The silica

spacer particles have previously been shown to have a diameter of 2.1 $\mu$m,[46,47] which then also sets the two-wall experiment gap dimension.

**Sample Cells.** Glass microscope coverslips (24 mm × 60 mm) were wiped clean with lens paper, and then sonicated for 30 min in acetone and 30 min in isopropanol before being soaked in Nochromix overnight. Small glass coverslips (18 mm × 18 mm) were wiped with lens paper and placed directly into Nochromix. All coverslips were rinsed with deionized (DI, 18.3 M$\Omega$) water and soaked in 0.1 M KOH for 30 min, and then rinsed with DI water again and dried with nitrogen before use.

O-Ring sample cells for one-wall experiments were constructed by using vacuum grease to adhere a 5 mm ID O-ring to a clean long coverslip. Afterward, dilute Au rod dispersions were pipetted into the O-ring, a small coverslip was placed on top and then sealed with vacuum grease. Confined cells were created by adding 10 $\mu$L of the Au/silica spacer particle mixture onto the center of a coverslip. A coverslip was placed on top of the droplet to confine particles between the two walls. Lens paper was used to wick away extraneous solution from between the coverslips until interference patterns were observed. The two coverslips were sealed together using epoxy.

Porous media sample cells were prepared by spin coating 100 $\mu$L of concentrated silica particle dispersion onto a long glass coverslip at 1000 rpm for 40 s. After spin coating, the coverslip was placed on a hot plate and dried overnight at 50 °C. Silica colloid coated coverslips were gently rinsed with DI water three to five times to remove any crystallized salt and then dried for 10 min on a hot plate. After drying, 12 $\mu$L of the Au rod stock was deposited onto the center of the coated coverslip and sealed in the same manner as the confined sample cells.

**Microscopy.** The two-wall experiments were performed using transmitted light on an upright microscope with a 63× objective (NA = 0.75). The one-wall and quasi-2D porous media experiments were performed on an inverted microscope with a 63× objective (NA = 0.75) using transmitted light and dark field, respectively. A dry dark field condenser attachment (NA = 0.8/0.95) was used to image experiments performed with concentrated porous media. Particle trajectories were monitored with a 12bit CCD camera in 4-binning mode for 30 000 frames at ≈27.6 fps for one-wall and two-wall experiments and at ≈10 fps for porous media experiments.

**Particle Tracking.** A new image analysis algorithm coded in FORTRAN 77 and MATLAB 2015a was developed to track particle translation and rotation. Rods appear dark on a bright background in transmitted light illumination (Figure 1C), and subsequent inversion (Figure 1D) and binary thresholding (Figure 1E) to identify all pixels comprising the rod. After identification of the coordinates of all pixels comprising a rod, $x_i$ and $y_i$, the coordinates of the center of mass (red points in Figure 1F) of each rod, $x_{cm}$ and $y_{cm}$, can be calculated as

$$x_{cm} = n^{-1} \sum_i^n x_i \tag{31}$$

$$y_{cm} = n^{-1} \sum_i^n y_i \tag{32}$$

Rod end points (green points in Figure 1F) were identified as the maximum distance from the center-of-mass coordinates and used to track the distance, $R_i$, and angle, $\theta_i$, of each end point as

$$R_i = [(x_{cm} - x_i)^2 + (y_{cm} - y_i)^2]^{0.5} \tag{33}$$

$$\theta_i = \arctan[(y_{cm} - y_i)/(x_{cm} - x_i)] \tag{34}$$

which were used to compute MSPD and MSAD curves using the eqs 17−19 and the multiple time origin method.[30] Figure 1G, H shows the magnitude of the center-of-mass position displacement and angular displacement vs time for a single rod. The instantaneous length of each rod is obtained by calculating the distance between the center and each end point and summing the two radii. The reported rod lengths are the most probable values obtained from histograms of all measured lengths for each particle.

For porous media experiments, a separate algorithm in MATLAB was used to identify silica microsphere positions and perimeters in dark field microscopy images using algorithms adapted for tracking cells.[48,49] The scheme is created by thresholding the silica particles based on a "solidity" factor (based on a percentage of white pixels). The solidity factor distinguishes the spheres, which appear as white halos around darker centers, from the much brighter Au rods. Boundaries were drawn around the silica particles that met the required solid percentage (but not around Au rods), which were overlaid in images and videos. The area fraction ($\phi$) of the image contained within the silica particle boundaries was also calculated.

## ■ RESULTS AND DISCUSSION

**Measuring Rod Translational and Rotation Diffusion.** Figure 2 shows mean squared positional displacements
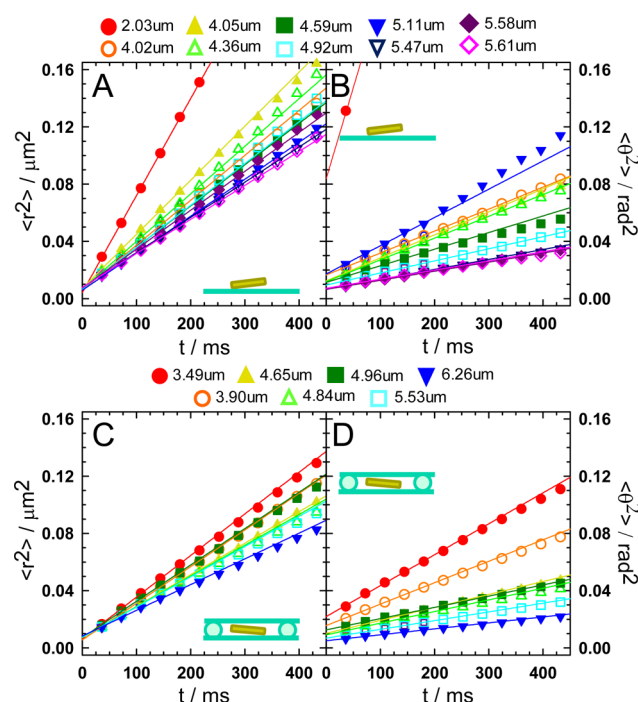


**Figure 2.** Mean square displacement date vs rod length and wall geometry. Mean squared (A, C) positional and (B, D) angular displacement vs time for Au colloidal rod particles with cross-sectional diameters of $d = 2a = 300$ nm. Results are reported for [NaCl] = 0.1 mM and varying rod lengths (see legend) adjacent to one wall (A, B) or confined between parallel walls separated by ≈2 $\mu$m (C, D). Symbols show particle tracking data, and lines are fits using eqs 18 and 19.

(MSPD) and mean squared angular displacements (MSAD) versus time from analyzing optical microscopy videos of ≈10 Au rods in 0.1 mM NaCl. Results are obtained for particles near a single wall, where they are confined by gravity, and for particles confined between two parallel walls separated by ≈2 $\mu$m diameter silica spacers. Each curve is fit via linear regression to eqs 18 and 19 to obtain $D^{t,i}$ and $D^{r,i}$. The measured values of $D^{t,i}$ and $D^{r,i}$ in Figure 2 show that shorter rods translate and rotate more quickly than longer rods having the same short-axis diameter (300 nm), consistent with expectations.

Deviations from the expected monotonic trends in Figure 2 may be the result of irregularities in the cylindrical rod shape, heterogeneities on the surfaces of the gold or silica, and spatiotemporal resolution limits in the experimental recordings. For example, blue triangles in Figure 2B correspond to a rod

having $L = 5.11 \mu m$ with a higher than expected rotational diffusion. In this specific instance, a slight curve to the rod shape may produce rolling motion at the rod ends that appears as faster rotation. In another case, the 4.02 and 4.05 $\mu m$ rods are simply two different rods, with lengths that are not significantly different relative to the image pixel size, and as such, differences in their measured diffusivities are also attributed to nonuniformities. Finally, the red circles for the shortest ~2 $\mu m$ rod in Figure 2 show an inadequate combination of spatial and temporal resolution necessary to capture the fast rotation of the smallest rod in this study. The last case is perhaps also most susceptible to out-of-plane 3D motion that could also make the apparent projected 2D rotation appear faster.

When comparing the two experimental geometries (one-wall versus two-walls) in Figure 2, the rods in the one-wall experimental system (Figure 2A) display faster translational diffusion than in the two-wall experiments (Figure 2C). The second confining wall ($\approx 2 \mu m$ separation) introduces an additional drag that can be expected to slow diffusion, consistent with expectations, results for spherical nanoparticles and nanotubes,[26,27,35] and simulations of anisotropic particles.[38] However, this effect is much less pronounced for rotational diffusion, which shows comparable rates for similar sized rods in both geometries (Figure 2B, D). Previous experiments have also observed limited effects of confinement on rotational diffusion.[34]

**Diffusivity vs Aspect Ratio, Ionic Strength, and Geometry.** Many measurements of particle diffusion for one-wall and two-wall configurations, like the ones reported in Figure 2, were performed versus ionic strength to vary how particles sample positions near the wall surface via differing strengths of electrostatic interactions.[26,27,35] Figure 3 reports diffusivities versus aspect ratio, $p = L/d$, from $p \approx 10$ to 20 (where $d = 2a = 300$ nm) and ionic strengths corresponding to deionized water ($\approx 0.03$ mM NaCl) up to 5 mM NaCl. Diffusivities for each of the four cases in Figure 3 were fit using the expressions in eqs 8−16, where the only adjustable parameter for each ionic strength was the elevation, $h$, of the Au rod above the surface. For the translational diffusivities in Figure 3A and C, the solid lines are least squared error fits, and the two types of dashed lines capture the maximum and minimum values necessary to enclose all data for each ionic strength. For the rotational diffusivities in Figure 3B and D, the theoretical curves are relatively insensitive to elevation and aspect ratio. As such, given the error bars in the measured data, we plot theoretical curves using the elevations fit to the translational diffusivities (rather than performing an independent least-squares fit to the measured rotational diffusivities). Using this approach, there is good agreement between the measurements and predictions. The fit values of $h$ for each case are reported in Figure 4.

The translational diffusion of rods is faster for shorter aspect ratios, lower ionic strength solutions, and one-wall configurations as shown by the theoretical curves in Figure 3A and C. For example, the DI and 0.1 mM diffusivities are $\approx 30\%$ higher for the one-wall than for the two-wall geometry, and the 1 and 5 mM conditions are $\approx 20\%$ higher for one-wall than two-wall configurations. There is also a decrease in the spread of the diffusivities measured, and thus the heights sampled by the rods, with the more confined geometry as is observed for both $D^t$ and $D^r$. As Figure 2 shows, the rotational diffusivities in Figure 3 exhibit a relative insensitivity to the one- or two-wall
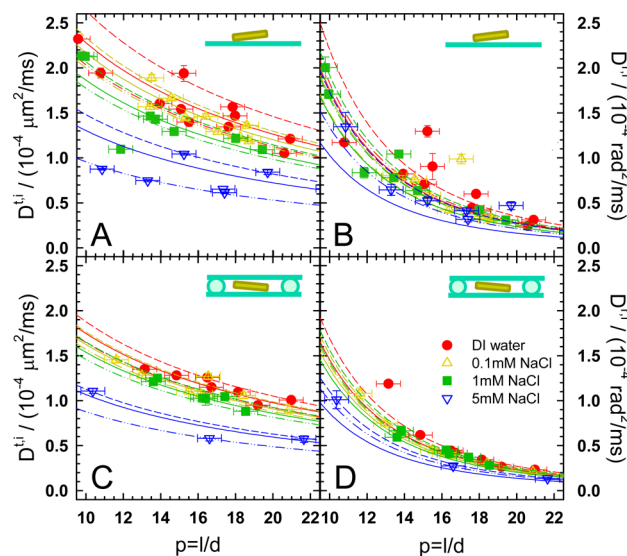


**Figure 3.** Rod diffusion vs solution ionic strength and wall geometry. Translational (A, C) and rotational (B, D) diffusion coefficients versus aspect ratio (abscissa) and ionic strength (see inset legend). The data points are the initial slopes of measured mean squared positional and angular displacements shown in Figure 2. For the translational diffusivities (A, C), the solid lines are least squared error fits to the $D^t$ using particle−wall separation, $h$, as the sole adjustable parameter in eq 12 for one wall and eq 15 for two walls; the dashed and dot-dot-dashed lines are the same equations fit to enclose the maximum and minimum values, respectively, within each ionic strength data set. For the rotational diffusivities (B, D), the lines are computed using the values of $h$ fit to translational diffusion data as input into eq 13 for one wall and eq 15 for two walls. Error bars are for each rod measured and are obtained as one pixel length at binning 4 (385 nm) for $p$, and the standard deviation of the slope in Figure 2 for $D^t$ and $D^r$.

configurations, but show a clear dependence on rod aspect ratio, as well as ionic strength.

The decreasing diffusivities for increasing ionic strength are the result of decreasing electrostatic repulsion that allows particles to approach wall surfaces more closely, and thus increases hydrodynamic resistance on particle motion. The decrease in translational diffusion is greater than the decrease in rotational diffusion, with particle−wall separation mediated by the solution ionic strength. This observed insensitivity in $D^r$ is consistent with a prior modeling study of rods as chains of spheres,[50] which is similar to the hydrodynamic model developed in our work.[38] The explanation for the difference between the separation dependence of the translational and rotational diffusivities can be explained by considering the rods as chains-of-spheres. Translation of chains-of-spheres are governed by the collective diffusion of the spheres comprising the chain, which decrease significantly with decreasing particle−wall separation. In contrast, rotation of chains-of-spheres depends on the diffusion of spheres relative to each other, which is insensitive to particle−wall separation for the elevations probed in this study.

**Measured vs Modeled Diffusivities.** The predicted diffusivities show good correspondence with the measured diffusivities for a single adjustable parameter, $h$. To test the accuracy of the fit separation estimates, and hence the elevation-dependent diffusivity models, we compare fits to predictions based on the conservative forces acting on the rods. Figure 4 shows the values of the rod particle−wall surface-to-surface separation from experiment and theory. Rod separations
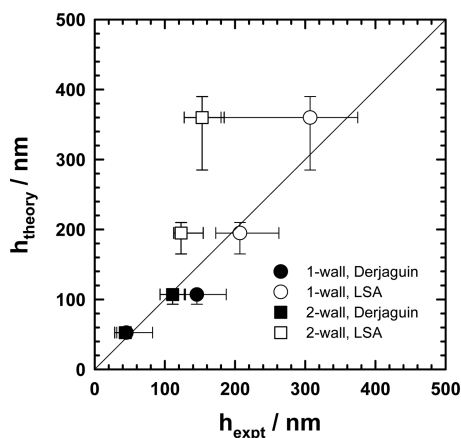
**Figure 4.** Rod—wall separations from measured diffusivity analysis vs colloidal force predictions. Values of particle—wall surface-to-surface separation from experiments, $h_{expt}$, in Figures 2 and 3 and from theoretical models, $h_{theory}$, using eqs 26 and 27. Values of $h_{expt}$ were obtained by fitting translational diffusivities near one wall (circles) to eq 12 and between two walls (squares) to eq 15. Error bars on $h_{expt}$ were obtained from the limiting lines in Figure 3 that contain all data points for each ionic strength. Values of $h_{theory}$ were obtained for double layers that are thin relative to the rod radius ($\kappa a \gg 1$; 1–5 mM, filled points) using eq 26 and for double layers that are comparable to the rod radius and particle separation ($\kappa a \approx \kappa h \approx 1$; 0.03–0.1 mM, open points) using eq 27 (based on conditions for most accurate models for electrostatic interactions between spheres[51]). Surface potentials used to compute $h_{theory}$ were chosen as $\psi_p = \zeta_p$ for the rod based on ionic strength dependent measurements in Figure 3 and as $\psi_w = -50$ mV for the glass slide with error bars based on low and high estimates of $-10$ and $-100$ mV.[52]

from fits to translational diffusion experiments, $h_{expt}$, for the one-wall and two-wall cases in Figure 3 are plotted on the x-axis, and separations from theoretical models, $h_{theory}$, using eqs 26 and 27 are shown on the y-axis.

Values of $h_{expt}$ are indicated as single points in Figure 4 and represent the best-fit separation for each $D^{t,i}$ versus $p$ curve for each ionic strength in Figure 3. The error bars in Figure 4 are taken from the extreme (dashed, dot-dot-dashed) curves of Figure 3. Values of $h_{theory}$ are computed using eq 26 for the higher ionic strengths ([NaCl] = 1 mM, 5 mM) and eq 27 for lower ionic strengths ([NaCl] = 0.03 mM, 0.1 mM), based on constraints determined by the relative thickness of the double layer to the rod radius, $\kappa a$, and rod—wall separation, $\kappa h$, as noted in the Theory section.[53] The points for $h_{theory}$ are based on wall surface potentials of $\psi_w = -50$ mV, obtained from prior measurements,[52] and error bars are based on more extreme surface potentials of $\psi_w = -10$ mV and $\psi_w = -100$ mV (with the rest of the model parameters reported in Table 1).

Agreement is good between the rod—wall separations inferred from model fits to translational diffusion data and predictions based on a balance of electrostatic repulsion and gravity (within error bars in Figure 4). This agreement is excellent at higher ionic strengths where the rod is closer to the bottom wall for both the one-wall and two-wall configurations. The agreement is worse (error bars do not account for discrepancies) for the systematically higher elevations predicted for the two-wall configuration at low ionic strengths. This could occur for a variety of reasons including (1) the electrostatic repulsion exerted by the top-wall is neglected in eq 27 and could cause particles to sample lower elevations than predicted, (2) the Brownian rotation perpendicular to the wall increases as

**Table 1. Constants Used in Theoretical Fits**

| variable (units) | value |
| --- | --- |
| $d = 2a$ ($\mu$m) | 0.3 |
| $\rho_p$ (g/cm$^3$) | 19.3 |
| $\rho_f$ (g/cm$^3$) | 1.00 |
| $\varepsilon_w$ | 78 |
| $T$ (K) | 294 |
| $\eta$ (Pa·s) | $1.002 \times 10^{-3}$ |
| $\delta$ ($\mu$m) | 2.1 |
| NaCl (mM) | $\approx$0.03, 0.1, 1, 5 |
| $\kappa^{-1}$ (nm) | 55, 27, 9.3, 4.3 |
| $\psi_p = \zeta_p$ (mV) | $-24, -24, -20, -15$ |
| $\psi_w$ (mV) | $-50$ |

it gets further away from the bottom wall; this effect is neglected (because it is nontrivial to include) both in terms of its influence on rod elevation as well as rod transport in the plane parallel to the bottom wall, and (3) the two-wall hydrodynamic correction in eq 16 based on one-wall is approximate (as discussed for spheres[26,35,54,55]), and could introduce some uncertainty in the elevation inferred from translational diffusion measurements.

As a final note, a rigorous consideration of the separation-dependent diffusion should include an average over all elevations[25,30] (eq 30) rather than a single elevation (e.g., most probable (eqs 26, 27) or average elevation (eq 28)). Although evaluation of $D(h)$ at a fixed elevation appears sufficient to generate agreement for most results in Figure 4, the potential energy ($U(h)$ in eq 29) could become asymmetric versus separation and include angular dependence (e.g., $U(h,\theta,\phi)$). A significantly different rod—wall interaction potential could cause the average over the probability ($p(h)$ in eq 29) to produce a value of $\langle D \rangle$ that is different from evaluating $D(h)$ at the mode or mean of $p(h)$. Such an effect could become more pronounced as particles move further from the bottom wall and also interact with the top wall. In any case, further efforts to test this idea by constructing models for a possible $U(h,\theta,\phi)$ are beyond the scope of the present work, and ultimately do not appear necessary to explain the agreement observed for the majority of the data in Figure 4. In short, diffusivities from evaluating the position dependent expressions at the most probable or average elevation, or by computing an average diffusivity over all sampled elevations, are all practically the same, with the exception of the low ionic strength cases.

**Translational Diffusion in Quasi-2D Porous Media.** Based on the agreement between experiments and models for rod diffusion near one and two walls, an experiment was designed to measure diffusion in quasi-2D porous media (Figure 5). These experiments measured short-time diffusion specifically as a probe of hydrodynamic interactions,[28,31,56,57] which are the main interest of this paper, without probing the role of pore microstructure on long-time diffusion (e.g., as studied by others[58,59]). Figure 5 shows trajectories and MSPD for translational diffusion of Au rods in very low ionic strength solution within a randomly oriented 2D porous media consisting of silica particles spin-coated onto a bottom coverslip and acting as spacers between a top coverslip. Similar to the two-wall case in Figures 2—4 (which is practically the infinitely dilute case for the experiments in Figure 5), the gap space is determined by the silica spacer particles to be $\approx$2.1 $\mu$m. Dark field microscopy was used to obtain contrast to simultaneously
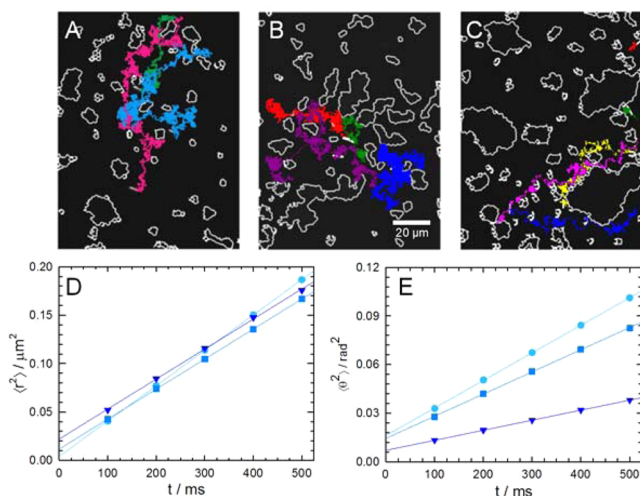
**Figure 5.** Short-time rod diffusion in quasi-2D porous media. Processed images from dark field microscopy experiments of Au rod diffusion in quasi-2D porous media with area fractions of (A) 0.085, (B) 0.156, and (C) 0.245. Colored trajectories of different Au rods illustrate translational diffusion in the course of the 50 min observation time. (D) MSPDs and (E) MSADs for the three blue trajectories in (A)−(C), which all correspond to rods of $L = 3.3-3.4$ $\mu$m with points indicating area factions of (circles) 0.085, (squares) 0.156, and (triangles) 0.245.

track Au particle diffusion and silica particle porous media boundaries.

Figure 5A−C shows trajectories for diffusion in quasi-2D porous media with area fractions of 0.085, 0.156, and 0.245. Overlaid in different colors are trajectories for individual rods for 50 min. Figure 5D shows short-time limit MSPDs for three rods with comparable lengths of ≈3.4 $\mu$m in Figure 5A−C designated by blue trajectories. For all three porous media area fractions tested, the resulting translational diffusivity is ≈$D = 2$ $\mu$m$^2$/ms, which is essentially the same as the two-wall results in Figure 3 for $p = l/d = 3.4$ $\mu$m/0.3 $\mu$m ≈ 11 and deionized water (where again, the results in Figure 3 are a quasi-2D porous media experiment with an area fraction near zero). Figure 5E shows short-time limit MSADs for the same three rods in Figure 5D. The resulting rotational diffusivities are near the two-wall results for the lowest area fraction but drop by a factor of ~3 for the highest area fraction investigated here. In short, the translational diffusivities for the three porous medium area fractions are not obviously distinguishable from each other, whereas the rotational diffusivities show a clear decrease with increasing area fraction.

The short-time translational diffusivity (Figure 5D) exhibits the hydrodynamic effects of the confining walls, but is insensitive to the local environments determined by the porous medium area fraction. This effect could arise from simply from averaging over rod positions far from the porous media surfaces that contribute to the net average diffusivity similar to the case without porous media. However, the reduced short-time rotational diffusivity (Figure 5E) with increasing area fraction indicates that interactions between rods and porous media surfaces do hinder rotational motion, which is perhaps to be expected. To explain both translational and rotational diffusivity trends in a self-consistent manner, electrostatic repulsion between the rod and porous media may produce alignment of the rod's long-axis parallel to the porous medium surface. As a result, rotation will be hindered, but the resulting translation

is dominated by this fastest diffusion mode for these configurations (eq 8).[60] This may be an example of how position and orientation are correlated, and how translational and rotational diffusion can be coupled,[16] as determined by interactions with the local porous media structure. This effect appears to produce about the same translational diffusivity in Figure 5 as confinement between two walls without porous media (Figure 3) (where the average motion parallel and perpendicular to the major axes determine the net diffusivity).

The long-time diffusivity for the trajectories in Figure 5A−C varies for the different quasi-2D porous media area fractions. However, in this initial study, we focused on the short-time behavior that is dominated by hydrodynamic interactions, which are relevant to the models being explored in this work. Practically, much more temporal and spatial sampling is required to obtain sufficient statistics and averaging of rod trajectories over locally heterogeneous media to obtain more general results for long-time diffusion.[61] It is also important to note that the short-time diffusivity investigated in this work, by necessity, always has a critical role in long-time diffusion; i.e., diffusion over longer times and distances necessarily requires many diffusive steps over short times and distances. For example, diffusion in dense suspensions[57] or porous media[62] includes a short-time diffusion term (accounting for local hydrodynamic interactions) multiplied by a term associated with long-time diffusion through surrounding microstructures (accounting for global energy landscapes). Our findings in this work on the role of hydrodynamic interactions in interfacial and confined diffusion of rod shaped colloidal particles can eventually be incorporated into more complex models for long-time diffusion that consider additional complexities of porous media microstructure (e.g., as studied by others[58,59]).

## ■ CONCLUSIONS

Measurements and models of interfacial and confined diffusion show agreement for different confinement geometries, rod aspect ratios, and electrostatic interactions. Measurements of translational and rotational diffusion of rods with aspect ratios of $p = l/d ≈ 10-20$ near one wall and confined between two walls agree quantitatively within the limits of uncertainty with models we developed to include position dependent hydrodynamic interactions. Significant reductions in translational and rotational diffusivities are observed as rod particles experience positions closer to boundaries. Aqueous solution ionic strength was investigated to mediate electrostatic repulsion between rods and surfaces. Ionic strength dependent diffusivities show that rod−wall separations predicted by theories for electrostatic repulsion (balanced by gravity) show good correspondence with separations inferred by fitting measured diffusivities to separation dependent models.

Finally, we show that short-time translational diffusion in quasi-2D porous media produces results nearly independent of porous media area fraction (whereas long-time diffusion is expected to be sensitive to porous media microstructure). In contrast, the short-time rotational diffusivity decreases with increasing porous media area fraction presumably due to rod interactions with porous media surfaces. The net neutral effect of porous media on short-time translation diffusion may be explained by hydrodynamic hindrance being compensated by faster translational diffusion along rod particles' long axes due to parallel alignment along porous media surfaces. Future studies will incorporate findings from this work on the role of hydrodynamic interactions on interfacial and confined diffusion

of rod particles into models for long-time diffusion that consider porous media microstructure. Ultimately, findings from this work provide a basis to interpret and predict colloidal rod transport in numerous applications relevant to biological, environmental, and synthetic material systems.

## ■ AUTHOR INFORMATION

**Corresponding Author**

*E-mail: mabevan@jhu.edu.

**ORCID** 

Howard Fairbrother: 0000-0003-4405-9728

Michael A. Bevan: 0000-0002-9368-4899

**Notes**

The authors declare no competing financial interest.

## ■ REFERENCES

(1) Berg, H. C. *Random Walks in Biology*; Princeton University Press: Princeton, NJ, 1993.

(2) Tavaddod, S.; Charsooghi, M. A.; Abdi, F.; Khalesifard, H. R.; Golestanian, R. Probing passive diffusion of flagellated and deflagellated Escherichia coli. *Eur. Phys. J. E: Soft Matter Biol. Phys.* **2011**, *34* (2), 1–7.

(3) Hunt, A. J.; Gittes, F.; Howard, J. The force exerted by a single kinesin molecule against a viscous load. *Biophys. J.* **1994**, *67* (2), 766–781.

(4) Li, G. L.; Tang, J. X. Diffusion of actin filaments within a thin layer between two walls. *Phys. Rev. E* **2004**, *69*, 061921.

(5) Geng, Y.; Dalhaimer, P.; Cai, S.; Tsai, R.; Tewari, M.; Minko, T.; Discher, D. E. Shape effects of filaments versus spherical particles in flow and drug delivery. *Nat. Nanotechnol.* **2007**, *2* (4), 249–255.

(6) Barua, S.; Yoo, J.-W.; Kolhar, P.; Wakankar, A.; Gokarn, Y. R.; Mitragotri, S. Particle shape enhances specificity of antibody-displaying nanoparticles. *Proc. Natl. Acad. Sci. U. S. A.* **2013**, *110* (9), 3270–3275.

(7) Weiss, T. H.; Mills, A. L.; Hornberger, G. M.; Herman, J. S. Effect of Bacterial Cell Shape on Transport of Bacteria in Porous Media. *Environ. Sci. Technol.* **1995**, *29* (7), 1737–1740.

(8) Liu, Q.; Lazouskaya, V.; He, Q.; Jin, Y. Effect of Particle Shape on Colloid Retention and Release in Saturated Porous Media. *J. Environ. Qual.* **2010**, *39* (2), 500–508.

(9) Salerno, M. B.; Flamm, M.; Logan, B. E.; Velegol, D. Transport of Rodlike Colloids through Packed Beds. *Environ. Sci. Technol.* **2006**, *40* (20), 6336–6340.

(10) Xu, S.; Liao, Q.; Saiers, J. E. Straining of Nonspherical Colloids in Saturated Porous Media. *Environ. Sci. Technol.* **2008**, *42* (3), 771–778.

(11) Fakhri, N.; MacKintosh, F. C.; Lounis, B.; Cognet, L.; Pasquali, M. Brownian Motion of Stiff Filaments in a Crowded Environment. *Science* **2010**, *330* (6012), 1804–1807.

(12) He, K.; Retterer, S. T.; Srijanto, B. R.; Conrad, J. C.; Krishnamoorti, R. Transport and Dispersion of Nanoparticles in Periodic Nanopost Arrays. *ACS Nano* **2014**, *8* (5), 4221–4227.

(13) Arpin, K. A.; Mihi, A.; Johnson, H. T.; Baca, A. J.; Rogers, J. A.; Lewis, J. A.; Braun, P. V. Multidimensional Architectures for Functional Optical Devices. *Adv. Mater.* **2010**, *22* (10), 1084–1101.

(14) Velev, O. D.; Gupta, S. Materials Fabricated by Micro- and Nanoparticle Assembly − The Challenging Path from Science to Engineering. *Adv. Mater.* **2009**, *21* (19), 1897–1905.

(15) Glotzer, S. C.; Solomon, M. J. Anisotropy of building blocks and their assembly into complex structures. *Nat. Mater.* **2007**, *6* (7), 557–562.

(16) Neild, A.; Padding, J. T.; Yu, L.; Bhaduri, B.; Briels, W. J.; Ng, T. W. Translational and rotational coupling in Brownian rods near a solid surface. *Phys. Rev. E* **2010**, *82* (4), 041126.

(17) Broersma, S. Viscous force and torque constants for a cylinder. *J. Chem. Phys.* **1981**, *74* (12), 6989–6990.

(18) Tirado, M. M.; de la Torre, J. G. Translational friction coefficients of rigid, symmetric top macromolecules. Application to circular cylinders. *J. Chem. Phys.* **1979**, *71* (6), 2581–2587.

(19) Tirado, M. M.; de la Torre, J. G. Rotational dynamics of rigid, symmetric top macromolecules. Application to circular cylinders. *J. Chem. Phys.* **1980**, *73* (4), 1986–1993.

(20) Brenner, H. Rheology of a dilute suspension of axisymmetric Brownian particles. *Int. J. Multiphase Flow* **1974**, *1* (2), 195–341.

(21) Wilcoxon, J.; Schurr, J. M. Dynamic light scattering from thin rigid rods: Anisotropy of translational diffusion of tobacco mosaic virus. *Biopolymers* **1983**, *22* (3), 849–867.

(22) Schumacher, G. A.; van de Ven, T. G. M. Brownian motion of rod-shaped colloidal particles surrounded by electrical double layers. *J. Chem. Soc., Faraday Trans.* **1991**, *87* (7), 971–976.

(23) Cush, R.; Dorman, D.; Russo, P. S. Rotational and Translational Diffusion of Tobacco Mosaic Virus in Extended and Globular Polymer Solutions. *Macromolecules* **2004**, *37* (25), 9577–9584.

(24) Mukhija, D.; Solomon, M. J. Translational and rotational dynamics of colloidal rods by direct visualization with confocal microscopy. *J. Colloid Interface Sci.* **2007**, *314* (1), 98–106.

(25) Bevan, M. A.; Prieve, D. C. Hindered Diffusion of Colloidal Particles Very Near to A Wall: Revisited. *J. Chem. Phys.* **2000**, *113* (3), 1228–1236.

(26) Eichmann, S. L.; Anekal, S. G.; Bevan, M. A. Electrostatically confined nanoparticle interactions and dynamics. *Langmuir* **2008**, *24*, 714–721.

(27) Eichmann, S. L.; Bevan, M. A. Direct Measurements of Protein Stabilized Gold Nanoparticle Interactions. *Langmuir* **2010**, *26*, 14409–14413.

(28) Beltran-Villegas, D. J.; Edwards, T. D.; Bevan, M. A. Self-Consistent Colloidal Energy and Diffusivity Landscapes in Macromolecular Solutions. *Langmuir* **2013**, *29* (40), 12337–12341.

(29) Zettner, C. M.; Yoda, M. Particle velocity field measurements in a near-wall flow using evanescent wave illumination. *Exp. Fluids* **2003**, *34*, 115–121.

(30) Anekal, S.; Bevan, M. A. Self Diffusion in Sub-Monolayer Colloidal Fluids Near a Wall. *J. Chem. Phys.* **2006**, *125*, 034906.

(31) Beltran-Villegas, D. J.; Sehgal, R. M.; Maroudas, D.; Ford, D. M.; Bevan, M. A. Fokker−Planck Analysis of Separation Dependent Potentials and Diffusion Coefficients in Simulated Microscopy Experiments. *J. Chem. Phys.* **2010**, *132*, 044707.

(32) Klein, J. D.; Clapp, A. R.; Dickinson, R. B. Direct measurement of interaction forces between a single bacterium and a flat plate. *J. Colloid Interface Sci.* **2003**, *261* (2), 379–385.

(33) Li, G.; Tang, J. X. Diffusion of actin filaments within a thin layer between two walls. *Phys. Rev. E* **2004**, *69* (6), 061921.

(34) Marshall, B.; Davis, V.; Lee, D.; Korgel, B. Rotational and translational diffusivities of germanium nanowires. *Rheol. Acta* **2009**, *48* (5), 589–596.

(35) Eichmann, S. L.; Smith, B.; Meric, G.; Fairbrother, D. H.; Bevan, M. A. Imaging Carbon Nanotube Interactions, Diffusion, and Stability in Nanopores. *ACS Nano* **2011**, *5* (7), 5909–5919.

(36) Jeffrey, D.; Onishi, Y. The slow motion of a cylinder next to a plane wall. *Q. J. Mech. Appl. Math.* **1981**, *34* (2), 129–137.

(37) Padding, J. T.; Briels, W. J. Translational and rotational friction on a colloidal rod near a wall. *J. Chem. Phys.* **2010**, *132* (5), 054511–8.

(38) Yang, Y.; Bevan, M. A. Interfacial Colloidal Rod Diffusion: Coefficients, Simulations & Analysis. *J. Chem. Phys.* **2017**, *147*, 054902.

(39) Tirado, M. M.; de la Torre, J. G. Translational friction coefficients of rigid, symmetric top macromolecules. Application to circular cylinders. *J. Chem. Phys.* **1979**, *71* (6), 2581–2587.

(40) Tirado, M. M.; Martinez, C. L.; de la Torre, J. G. Comparison of theories for the translational and rotational diffusion coefficients of rod-like macromolecules. Application to short DNA fragments. *J. Chem. Phys.* **1984**, *81* (4), 2047−2052.

(41) Happel, J.; Brenner, H. *Low Reynolds Number Hydrodynamics*; Prentice-Hall: Englewood Cliffs, NJ, 1965.

(42) Wu, H.-J.; Everett, W. N.; Anekal, S. G.; Bevan, M. A. Mapping Patterned Potential Energy Landscapes with Diffusing Colloidal Probes. *Langmuir* **2006**, *22*, 6826−6836.

(43) Israelachvilli, J. *Intermolecular and Surface Forces*, 3rd ed.; Academic Press: New York, 2011.

(44) Adamczyk, Z.; Warszynski, P. Role of electrostatic interactions in particle adsorption. *Adv. Colloid Interface Sci.* **1996**, *63*, 41−149.

(45) Yu, J.-S.; Kim, J. Y.; Lee, S.; Mbindyo, J. K. N.; Martin, B. R.; Mallouk, T. E. Template synthesis of polymer-insulated colloidal gold nanowires with reactive ends. *Chem. Commun.* **2000**, *24*, 2445−2446.

(46) Wu, H.-J.; Bevan, M. A. Direct Measurement of Single and Ensemble Average Particle-Surface Potential Energy Profiles. *Langmuir* **2005**, *21* (4), 1244−1254.

(47) Wu, H.-J.; Pangburn, T. O.; Beckham, R. E.; Bevan, M. A. Measurement and Interpretation of Particle−Particle and Particle−Wall Interactions in Levitated Colloidal Ensembles. *Langmuir* **2005**, *21* (22), 9879−9888.

(48) Duncan, G. A.; Fairbrother, D. H.; Bevan, M. A. Diffusing colloidal probes of cell surfaces. *Soft Matter* **2016**, *12* (21), 4731−4738.

(49) Duncan, G. A.; Gerecht, S.; Fairbrother, D. H.; Bevan, M. A. Diffusing Colloidal Probes of kT-Scale Biomaterial−Cell Interactions. *Langmuir* **2016**, *32* (46), 12212−12220.

(50) Lele, P. P.; Swan, J. W.; Brady, J. F.; Wagner, N. J.; Furst, E. M. Colloidal diffusion and hydrodynamic screening near boundaries. *Soft Matter* **2011**, *7* (15), 6844−6852.

(51) Glendinning, A. B.; Russel, W. B. The electrostatic repulsion between charged spheres from exact solutions to the linearized poisson-boltzmann equation. *J. Colloid Interface Sci.* **1983**, *93* (1), 95−104.

(52) Bitter, J. L.; Duncan, G. A.; Beltran-Villegas, D. J.; Fairbrother, D. H.; Bevan, M. A. Anomalous Silica Colloid Stability and Gel Layer Mediated Interactions. *Langmuir* **2013**, *29*, 8835−8844.

(53) Russel, W. B.; Saville, D. A.; Schowalter, W. R. *Colloidal Dispersions*; Cambridge University Press: New York, 1989.

(54) Ganatos, P.; Pfeffer, R.; Weinbaum, S. A strong interaction theory for the creeping motion of a sphere between plane parallel boundaries. Part 2. Parallel motion. *J. Fluid Mech.* **1980**, *99*, 755−783.

(55) Pawar, Y.; Anderson, J. L. Hindered Diffusion in Slit Pores: An Analytical Result. *Ind. Eng. Chem. Res.* **1993**, *32*, 743−746.

(56) Medina-Noyola, M. Long-Time Self-Diffusion in Concentrated Colloidal Dispersions. *Phys. Rev. Lett.* **1988**, *60* (26), 2705−2708.

(57) Brady, J. F. The Long-Time Self-Diffusivity in Concentrated Colloidal Dispersions. *J. Fluid Mech.* **1994**, *272*, 109−133.

(58) He, K.; Babaye Khorasani, F.; Retterer, S. T.; Thomas, D. K.; Conrad, J. C.; Krishnamoorti, R. Diffusive Dynamics of Nanoparticles in Arrays of Nanoposts. *ACS Nano* **2013**, *7* (6), 5122−5130.

(59) Skaug, M. J.; Wang, L.; Ding, Y.; Schwartz, D. K. Hindered Nanoparticle Diffusion and Void Accessibility in a Three-Dimensional Porous Medium. *ACS Nano* **2015**, *9* (2), 2148−2156.

(60) Han, Y.; Alsayed, A. M.; Nobili, M.; Zhang, J.; Lubensky, T. C.; Yodh, A. G. Brownian Motion of an Ellipsoid. *Science* **2006**, *314* (5799), 626−630.

(61) Elliott, L. C. C.; Barhoum, M.; Harris, J. M.; Bohn, P. W. Trajectory analysis of single molecules exhibiting non-Brownian motion. *Phys. Chem. Chem. Phys.* **2011**, *13* (10), 4326−4334.

(62) Saxton, M. J. Lateral Diffusion in an Archipelago - Single-Particle Diffusion. *Biophys. J.* **1993**, *64* (6), 1766−1780.